remote sensing

MDPI

Article

AIRS and MODIS Satellite-Based Assessment of Air Pollution in Southwestern China: Impact of Stratospheric Intrusions and Cross-Border Transport of Biomass Burning

Puyu Lian [1], Kaihui Zhao [2,*] and Zibing Yuan [1]

[1] School of Environment and Energy, South China University of Technology, Guangzhou 510006, China; espuyu@mail.scut.edu.cn (P.L.); zibing@scut.edu.cn (Z.Y.)
[2] Yunnan Key Laboratory of Meteorological Disasters and Climate Resources in the Greater Mekong Subregion, Yunnan University, Kunming 650091, China
* Correspondence: khzhao@ynu.edu.cn; Tel.: +86-177-9100-8508

Abstract: The exacerbation of air pollution during spring in Yunnan province, China, has attracted widespread attention. However, many studies have focused solely on the impacts of anthropogenic emissions while ignoring the role of natural processes. This study used satellite data spanning 21 years from the Moderate Resolution Imaging Spectroradiometer (MODIS) and the Atmospheric Infrared Sounder (AIRS) to reveal two natural processes closely related to springtime ozone (O_3) and $PM_{2.5}$ pollution: stratospheric intrusions (SIs) and cross-border transport of biomass burning (BB). We aimed to assess the mechanisms through which SIs and cross-border BB transport influence O_3 and $PM_{2.5}$ pollution in Southwestern China during the spring. The unique geographical conditions and prevalent southwest winds are considered the key driving factors for SIs and cross-border BB transport. Frequent tropopause folding provides favorable dynamic conditions for SIs in the upper troposphere. In the lower troposphere, the distribution patterns of O_3 and stratospheric O_3 tracer (O_3S) are similar to the terrain, indicating that O_3 is more likely to reach the surface with increasing altitude. Using stratospheric tracer tagging methods, we quantified the contributions of SIs to surface O_3, ranging from 6 to 31 ppbv and accounting for 10–38% of surface O_3 levels. Additionally, as Yunnan is located downwind of Myanmar and has complex terrain, it provides favorable conditions for $PM_{2.5}$ and O_3 generation from cross-border BB transport. The decreasing terrain distribution from north to south in Yunnan facilitates $PM_{2.5}$ transport to lower-elevation border cities, whereas higher-elevation cities hinder $PM_{2.5}$ transport, leading to spatial heterogeneity in $PM_{2.5}$. This study provides scientific support for elucidating the two key processes governing springtime $PM_{2.5}$ and O_3 pollution in Yunnan, SIs and cross-border BB transport, and can assist policymakers in formulating optimal emission reduction strategies.

Keywords: AIRS and MODIS satellites; aerosol; stratospheric intrusions; biomass burning; $PM_{2.5}$ and O_3 pollution; Southwestern China

Citation: Lian, P.; Zhao, K.; Yuan, Z. AIRS and MODIS Satellite-Based Assessment of Air Pollution in Southwestern China: Impact of Stratospheric Intrusions and Cross-Border Transport of Biomass Burning. *Remote Sens.* **2024**, *16*, 2409. https://doi.org/10.3390/rs16132409

Academic Editor: Costas Varotsos

Received: 15 April 2024
Revised: 26 June 2024
Accepted: 26 June 2024
Published: 1 July 2024

1. Introduction

Elevated amounts of $PM_{2.5}$ (particulate matter with an aerodynamic equivalent diameter of 2.5 μm or less) and ozone (O_3) are currently the two major bottleneck issues constraining the continuous improvement of air quality in China. The complexity of their source mechanisms has brought enormous challenges to the prevention and control of air pollution. Although implementing the Air Pollution Prevention and Control Action Plan (APPCAP) has effectively controlled $PM_{2.5}$ pollution in most parts of China, the emphasis on reducing $PM_{2.5}$ emissions has led to a continuous increase in O_3 concentrations. In some areas, this has resulted in combined pollution from $PM_{2.5}$ and O_3 [1,2]. Owing to its harmful impact on human health, vegetation growth, and climate change [3,4], the

synergistic control of O_3 and $PM_{2.5}$ constitutes a critical priority in China's long-term air quality management agenda.

The main sources of $PM_{2.5}$ depend on local primary emissions, secondary photochemical reactions, and regional transport. Industrial, traffic, and residential sources can directly emit $PM_{2.5}$ [5]. Meanwhile, these sources also release other pollutants, which undergo various chemical and physical processes to transform into sulfate, nitrate, and secondary organic aerosols, constituting fine particulate matter [6,7]. Numerous studies have used source apportionment, numerical simulations, and other methods to quantify the contributions of primary emissions and secondary generation to $PM_{2.5}$ during high-pollution events [8–11]. Apart from local sources, regional transport is another significant contributor to local $PM_{2.5}$ pollution, and it can directly carry large amounts of pollutants from other areas, exacerbating local air pollution [12–14]. Under specific meteorological conditions, regional transport plays a dominant role in $PM_{2.5}$ pollution events in regions such as the North China Plain (NCP), the Sichuan Basin (SCB), and the Yunnan Plateau (YP), with contribution rates reaching exceptionally high levels [12,15,16]. Zhang et al. [17] investigated the difference in $PM_{2.5}$ transport flux between NCP and SCB in autumn and winter. They observed that NCP was controlled by a cold front weather system and transported $PM_{2.5}$ to surrounding areas. In contrast, $PM_{2.5}$ in SCB was affected by interbasin transport because of the complex terrain that hindered horizontal diffusion. Unlike the other two regions, $PM_{2.5}$ in YP was found to be influenced by biomass burning (BB) in the Indo-China Peninsula during spring, a source of cross-border BB transport [16,18].

Unlike $PM_{2.5}$ pollution, O_3 is a secondary pollutant primarily formed through local photochemical reactions. These reactions involve interactions between precursor pollutants, such as nitrogen oxides (NO_x) and volatile organic compounds (VOCs), in the presence of solar radiation. Influenced by anthropogenic and natural emissions, the local photochemical environment plays an important role in shaping O_3 concentrations [19,20]. Additionally, regional transport from neighboring areas and stratospheric intrusions (SIs) are also important O_3 budget sources [21]. Regional transport is a driving factor behind surface O_3 pollution in regions like Beijing–Tianjin–Hebei (BTH), the Yangtze River Delta (YRD), and the Pearl River Delta (PRD) [15,22,23]. SIs involve the downward transport of O_3 from the stratosphere to the troposphere and even the surface, under the influence of physical mechanisms such as tropopause folding, cut-off lows, subtropical jet streams, and wave breaking [24–27]. Under specific meteorological conditions such as typhoons, tropical cyclones, and subtropical highs, local circulation intensifies, leading to enhanced regional transport and SIs, impacting the near-surface O_3 concentration [28–30].

Compared with plains such as the BTH, the YRD, and the PRD, Yunnan boasts a unique and complex topography as a high-altitude plateau with substantial elevation variations among its cities. While Yunnan's overall altitude is relatively high, a considerable difference in elevation exists among its cities, creating a topographical landscape with higher elevations in the northwest and lower elevations in the southeast, resulting in a stair-step descent from south to north. Additionally, the climate of Yunnan is characterized by its complexity in both the horizontal and vertical dimensions, featuring a combination of boreal, temperate, and tropical climates, and temperature variations are notably influenced by changes in elevation. In contrast to the other major city clusters, such as BTH, the YRD, and the PRD, where $PM_{2.5}$ pollution is concentrated in winter and O_3 pollution is concentrated in summer [12,20,31], Yunnan experiences $PM_{2.5}$ and O_3 pollution primarily during spring. High-frequency tropopause folding provides favorable dynamic conditions for the downward transport of O_3-rich air mass from the stratosphere to the troposphere during springtime, influencing near-surface O_3 concentrations [25,30,32]. Additionally, BB is active in the spring over the Indo-China Peninsula (ICP), and the prevailing westerly winds transport BB-generated $PM_{2.5}$ and O_3 to Yunnan [33,34]. Numerous studies of pollution cases have confirmed the existence of transport channels between Yunnan and the ICP [16,18]. Given the unique topographic conditions and geographical location of Yunnan, these two distinct transport processes, SIs and cross-border BB transport, exert a

more profound impact on $PM_{2.5}$ and O_3 pollution in Yunnan during the spring. However, current emission reduction policymaking has predominantly focused on reducing local anthropogenic sources, and there remains a notable lack of research on the impact of these two natural sources on the mechanism of springtime O_3 pollution in Yunnan.

Satellite remote sensing technology can provide vertical profile data, real-time observations, and extensive spatiotemporal coverage, which can help to better understand the mechanisms governing $PM_{2.5}$ and O_3 pollution [35–37]. Instruments such as the Moderate Resolution Imaging Spectroradiometer (MODIS), the Ozone Monitoring Instrument (OMI), and Cloud–Aerosol Lidar and Infrared Satellite Observations (CALIPSO) have been widely used to retrieve the spatiotemporal distribution of Aerosol Optical Depth (AOD), which quantifies the solar attenuation caused by aerosols [38–40]. Shaik et al. [41] and others have confirmed the accuracy of MODIS-derived AOD by comparing it to ground-based AOD, showing strong agreement with a correlation coefficient (R) of 0.86 and a root mean square error (RMSE) of 0.14. Additionally, satellite-based AOD has been instrumental in revealing the impact of BB on the optical properties and vertical structure of aerosols [35,42]. Satellite-based vertical profiles of O_3, obtained from instruments like the Atmospheric Infrared Sounder (AIRS), are crucial for investigating SIs [43,44]. Ma et al. [45] used vertical AIRS profiles of O_3 to provide evidence of SIs in cities such as Chaoyang, Shijiazhuang, and Hangzhou during the spring and summer of 2019. By characterizing the three-dimensional spatiotemporal distribution of pollutants, satellite observations can significantly enhance our understanding of pollutant transport processes and largely compensate for a lack of vertical observation data.

To study and quantify the impact of SIs and cross-border BB transport on O_3 and $PM_{2.5}$ concentrations in Yunnan province during spring, 21-year satellite observations from MODIS and AIRS were used to investigate the spatial and temporal variations in O_3 and $PM_{2.5}$. The Whole Atmosphere Community Climate Model (WACCM) dataset was used to quantify the contributions of SIs and cross-border BB transport to O_3 and $PM_{2.5}$ concentrations under complex topographic conditions. Finally, the sources of $PM_{2.5}$ and O_3 in Yunnan during spring were determined by using the Hybrid Single Particle Lagrangian Integrated Trajectory (HYSPLIT) model to simulate air mass trajectories. The objectives of this study are to: (1) analyze the general characteristics of O_3 and AOD; (2) explain the mechanisms of SIs and cross-border BB transport; and (3) investigate the influence of SIs and cross-border BB transport on O_3 and $PM_{2.5}$ under complex topographic conditions.

2. Materials and Methods

2.1. Studied Area

Two nested domains were used in this study: the 16°–36°N, 85°–125°E region, and Yunnan province (Figure 1). Previous studies indicate that the westerly jet stream is an important midlatitude circulation in region d01 during the spring [33]. This area is known for frequent tropopause folding and is also a hotspot for BB during the spring [32].

2.2. Satellite Datasets

We used two types of satellite datasets from different instruments, MODIS and AIRS. Tables 1 and 2, respectively, present their instrument specifications and the attributes of their corresponding datasets.

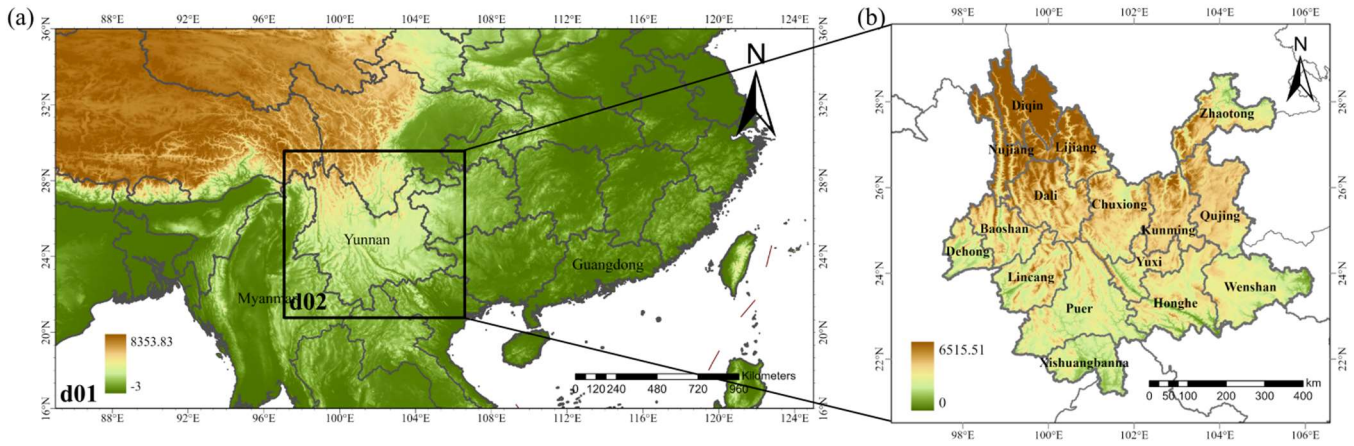

Figure 1. Elevation map of studied area: (**a**) the 16°–36°N, 85°–125°E region, (**b**) Yunnan province.

Table 1. Specifications of MODIS and AIRS instruments.

Instrument/ Satellite	Wavelength Bands	Number of Bands	Spectral Resolutions	Temporal Resolution	Spatial Resolution
MODIS/Aqua	0.4–14.4 μm	Bands 1–19 and 26 Bands 20–25 and 27–36	0.4 μm to 2.2 μm 3.66 μm to 14.4 μm	Multiple times daily	250 m, 500 m and 1000 m
AIRS/Aqua	0.4–15.4 μm	2378 infrared channels	649 to 1136 cm^{-1} (longwave) 1213 to 1613 cm^{-1} (midwave) 2181 to 2665 cm^{-1} (shortwave)	Twice daily	1° × 1°
		4 visible/near-infrared channels	0.4 μm to 0.94 μm		

Table 2. Attributes of the satellite datasets used in this study.

Instrument/ Satellite	Data Provider	Data Product	Temporal Resolution	Spatial Resolution	Parameters Used	Reference
MODIS/Aqua	LAADS	MYD04_L2	Daily (2003–2023)	10 km × 10 km	AOD (550 nm)	(Levy et al., Sayer et al.) [46,47]
AIRS/Aqua	GESDISC	AIRS3STM 7.0	Monthly (2003–2023)	1° × 1°	O_3 profile	(Aumann et al.) [48]

2.2.1. MODIS

MODIS is part of the National Aeronautics and Space Administration (NASA) and is deployed on two satellites, Aqua and Terra, which are in near-polar orbits. This positioning allows for global observations multiple times a day. MODIS captures data in 36 inter-aligned spectral bands ranging from 0.4 μm to 14.4 μm and acquires them at three spatial resolutions: 250 m, 500 m, and 1000 m, providing global data over a wide range. The daily level 2 Collection 6.1 AOD dataset (MYD04_L2) is used to provide AOD data, which are available from the website: https://ladsweb.modaps.eosdis.nasa.gov/, accessed on 3 November 2023. Each file in this dataset corresponds to a 5-min MODIS orbital fragment with a spatial resolution of 10 × 10 km, containing a total of 203 × 135 pixels. The MODIS retrieval algorithm for aerosol properties is divided into the Dark Target (DT) and Deep Blue (DB) algorithms. The DT algorithm is used for retrieving AOD over the ocean and vegetated land, while the DB algorithm is designed for bright surfaces, like deserts and urban areas, and dark surfaces, including vegetated regions. The latest MODIS product

merges the strengths of the DT and DB algorithms into a new combined dataset that relies on the Normalized Difference Vegetation Index (NDVI). The combined dataset is generated as follows: (1) if NDVI > 0.3, DT retrievals are used; (2) if NDVI < 0.2, DB retrievals are used; (3) if 0.2 $\leq$ NDVI $\leq$ 0.3, the average of the DT and DB retrievals is used, or the one with the recommended quality assurance (QA = 3 for DT and QA $\geq$ 2 for DB) is selected. This approach enhances spatial coverage over land, particularly in transitional regions with low vegetation that are dark enough for the DT algorithm to be applicable [49]. Consequently, we used the combined dataset to analyze the general characteristics of AOD, namely, "AOD_550_Dark_Target_Deep_Blue_ Combined".

2.2.2. AIRS

AIRS was launched with the Aqua satellite on 4 May 2002, as part of NASA. This sensor is specifically designed to obtain infrared spectral information in the atmosphere; it has a high spectral resolution and provides all-day vertical profile observations. Furthermore, the AIRS and MODIS instruments are concurrently deployed on the Aqua satellite, establishing a dual-satellite configuration that comprehensively analyzes both surface and atmospheric data. In this study, the AIRS Version 7 Level 3 standard product with 1° × 1° spatial resolution and monthly temporal resolution was used to investigate the spatiotemporal distribution of O_3. The vertical profile data are divided into 24 pressure levels, from 1000 hPa to 1 hPa, and can be obtained from the website: https://airs.jpl.nasa.gov/data/get-data/standard-data/, accessed on 3 November 2023.

2.3. WACCM Simulation

2.3.1. WACCM Datasets

The WACCM is a global climate model developed by the National Center for Atmospheric Research (NCAR), falling under the Atmospheric Chemistry-Climate Model (AOGCM) category. This model aims to simulate and study physical and chemical processes in the atmosphere, covering entire pressure levels from the surface to the top of the atmosphere. This model uses anthropogenic emissions from the latest Copernicus Atmosphere Monitoring Service (CAMS) inventory. Open-flame emissions are derived from FINN-v1. The spatial resolution of the datasets is 0.9° × 1.25°, and the vertical profile is divided into 88 levels, which can be obtained from the website: https://www.acom.ucar.edu/waccm/download.shtml, accessed on 3 November 2023. The stratospheric O_3 tracer (O_3S) and the CO tracer (CO01) represent the contribution of SIs to tropospheric O_3 and the impact of global BB emissions on local CO.

2.3.2. Model Evaluation

O_3 and $PM_{2.5}$ observations from site data and AOD observations from the MODIS dataset are performed to assess the performance of the WACCM dataset at eight sites in Yunnan from 2020 to 2023. The hourly O_3 and $PM_{2.5}$ data from 2020 to 2023 used in this study were obtained from the China Environmental Monitoring Center's national urban air quality real-time release platform (https://air.cnemc.cn:18007/, accessed on 3 November 2023). Figure S1 and Table S1 show that the WACCM dataset had good performance for O_3, $PM_{2.5,}$ and AOD, with averaged R of 0.86, 0.88, and 0.67, respectively. The averaged RMSEs are 14.21 μg/m^3, 23.17 μg/m^3, and 0.21, and the mean biases (MBs) are 11.27 μg/m^3, 12.29 μg/m^3, and 0.14, respectively. Overall, the above discussion can prove the reliability of WACCM data and support the subsequent analysis of our study objectives.

2.4. HYSPLIT Model

The HYSPLIT model is a Lagrangian trajectory model developed by the National Oceanic and Atmospheric Administration (NOAA) to calculate simple air parcel trajectories as well as complex simulations for transportation, dispersion, chemical transformation, and deposition. The HYSPLIT model has been widely used to track aerosol sources and identify BB emission smoke delivery routes [18,35]. The Global Data Assimilation System

(GDAS) from the National Centers for Environmental Prediction (NCEP) is used to generate meteorological conditions at an interval of 6 h with 1° horizontal resolution and 23 vertical levels from 1000 hPa to 20 hPa, and its data can be obtained from the website: https://www.ready.noaa.gov/data/archives/gdas1/, accessed on 3 November 2023. Two representative cities, Kunming (25.04°N, 102.66°E) and Xishuangbanna (22.02°N, 100.80°E), were selected as the model-simulated trajectory termination or particle receiving points. The starting height was set to 500 m above ground level, and simulations were conducted at 00:00, 06:00, 12:00, and 18:00 UTC during spring from 2020 to 2023 for 72 h backward in time. After running the HYSPLIT model, we obtained trajectory information, including the number of trajectories and endpoints within each grid cell that the trajectory passed through.

Potential Source Contribution Function (PSCF) analysis is widely used to identify spatial patterns in pollution sources and quantitatively estimate the relative contribution strengths of different source areas [18,31,50]. To assess the pollution levels in the study region from various source areas, it was essential to establish threshold values for $PM_{2.5}$. According to the daily average primary limit of the Ambient Air Quality Standards of China (GB 3095-2012) [51], the $PM_{2.5}$ threshold value was set to 35 $\mu g/m^3$. The position where each trajectory endpoint falls is recorded as (i, j). Mij represents the number of trajectory endpoints where the measured $PM_{2.5}$ parameter exceeds the threshold value within the ij-th grid cell, and Nij represents the total number of trajectory endpoints within the ij-th grid cell. The PSCF value of each grid cell in the study area was determined by calculating the ratio of M_{ij} and N_{ij}, as shown in Equation (1):

$$P_{ij} = \frac{M_{ij}}{N_{ij}} \quad (1)$$

When N_{ij} is small, the uncertainty of the conditional probability P_{ij} increases. To reduce this uncertainty, we referred to the study by Polissar [50] and introduced a weight function, W_{ij}, which is multiplied by P_{ij}, as follows:

$$W_{ij} = \begin{cases} 1.00 & 150 < N_{ij} \\ 0.70 & 15 < N_{ij} \leq 150 \\ 0.42 & \cdots\cdots \quad 5 < N_{ij} \leq 15 \\ 0.17 & N_{ij} \leq 5 \end{cases} \quad (2)$$

$$WPSCF = W_{ij} \times P_{ij} \quad (3)$$

Concentration-Weighted Trajectory (CWT) analysis was employed to determine the potential source area contributions of $PM_{2.5}$. $PM_{2.5}$ concentrations in the target cities can be obtained from the China Environmental Monitoring Center's national urban air quality real-time release platform (https://air.cnemc.cn:18007/, accessed on 3 November 2023). The CWT value of each grid cell in the study area was obtained by calculating the weighted value of pollutant concentration in different trajectories, as shown in Equation (4):

$$C_{ij} = \frac{1}{\sum_{l=1}^{M} T_{ijl}} \sum_{l=1}^{M} C_l T_{ijl} \quad (4)$$

where: C_{ij} represents the average weighted $PM_{2.5}$ concentration of the ij-th grid cell ($\mu g/m^3$); l is the number of trajectories; M is the total number of trajectories; C_l represents the pollutant concentration along trajectory l; and T_{ijl} represents the time spent by trajectory l in the ij-th grid cell. Similar to P_{ij}, we used W_{ij} to decrease the error in C_{ij}, as follows:

$$WCWT = W_{ij} \times C_{ij} \quad (5)$$

3. Results

3.1. General Characteristics of AOD and O_3

To compare the difference in the effects of cross-border BB transport and SIs on $PM_{2.5}$ and O_3 in Yunnan and the entire region, this section analyzes satellite observations from MODIS and AIRS in d01 and d02, as shown in Figure 1.

We analyzed the seasonal variation characteristics of AOD using MODIS satellite observations from 2003 to 2023, aiming to indirectly obtain the variation characteristics of $PM_{2.5}$ from an observational perspective. Figure 2 depicts the seasonally averaged AOD over Yunnan province from 2003 to 2023. In the Yunnan region, AOD exhibits distinctive characteristics, with its peak occurring during the spring season. This feature contrasts notably with other regions, such as BTH and the YRD, where the maximum AOD can be observed during the summer season [52,53]. The average AOD during spring has consistently exceeded the 21-year mean value, with 16 years recording maximum AOD values in spring surpassing 0.8 and even reaching 1.1. This phenomenon became more pronounced after 2015, with AOD values in spring significantly surpassing those of other seasons. Notably, the high AOD values during spring in Yunnan are more pronounced compared with the overall region, with the average falling within a range of 0.35–0.47.

Figure 2. MODIS satellite retrieval of 550 nm AOD over (**a**) Yunnan province and (**b**) the 16°–36°N, 85°–125°E region from 2003 to 2023. The red lines depict the change in the annual mean of AOD from 2003 to 2023. The black-dashed lines depict the average AOD from 2003 to 2023.

Additionally, $PM_{2.5}$, PM_{10}, and O_3 and AOD exhibit similar seasonal variation characteristics, with their peak values appearing in spring. However, there are significant differences in the annual variation trends of these elements in Yunnan province between 2015 and 2023, with $PM_{2.5}$ and PM_{10} decreasing by 4 $\mu g/m^3$ and 12 $\mu g/m^3$, respectively,

and O_3 increasing by 13 μg/m^3. The APPCAP plan's implementation in 2013 is responsible for these variations. Reductions in anthropogenic emissions have led to a sustained decrease in $PM_{2.5}$ and PM_{10} emissions. Besides the increase in radiative flux due to the decrease in $PM_{2.5}$ exacerbating O_3 pollution, the change in pollutant emission structure caused by China's $PM_{2.5}$ control-focused emission reduction measures may be a significant reason for the recent continuous rise in O_3 pollution [54]. Meanwhile, AOD did not change significantly, fluctuating around a value of 1. Previous studies have shown that $PM_{2.5}$ and PM_{10} contribute to the total aerosol load, thus affecting AOD in the atmosphere [55–57]. Figure S3 shows that there is a positive relationship between $PM_{2.5}$, PM_{10}, and AOD in spring and summer over Yunnan, with an R ranging from 0.56 to 0.75, indicating that $PM_{2.5}$ and PM_{10} significantly contribute to springtime and summertime AOD in Yunnan. However, the correlations between $PM_{2.5}$, PM_{10}, and AOD are low in autumn and winter, which are attributed to various meteorological factors such as humidity, wind speed, and atmospheric stability. For instance, high humidity can cause hygroscopic particle growth, increasing AOD, but this does not necessarily indicate a proportional increase in surface $PM_{2.5}$ or PM_{10}. Additionally, AOD signifies the cumulative extinction capacity of all aerosol particles within the vertical atmospheric column. However, $PM_{2.5}$ and PM_{10} site observations can only reflect surface pollution levels. The differences mentioned above can lead to variations in the correlation between satellite observations of AOD and surface observations of $PM_{2.5}$ or PM_{10} in different seasons.

In the context of significant annual reductions in $PM_{2.5}$ and PM_{10} pollution, the consistently high levels of $PM_{2.5}$ in spring are particularly notable. Consequently, the impact of cross-border BB transport occurring during spring has been further amplified. Furthermore, the overall increase in spring AOD in Yunnan and the entire region confirms the homogeneity of AOD sources in these two areas.

Figure 3 depicts the spatiotemporal distribution of O_3 in Yunnan and the entire region. A tongue-shaped plume of high O_3 can be seen extending from 100 hPa downward to the lower troposphere, with O_3 concentrations higher than 80.0 ppbv. The downward transport of stratospheric O_3-enriched air accumulates at the top of the boundary layer owing to the blocking effect of that layer, forming an area of high O_3 values. Previous studies have proved that similar phenomena can indicate the occurrence of SIs [21,25]. The latitude cross-section also further supports that SIs transport O_3-enriched air from the stratosphere to the troposphere, forming a tropospheric O_3 hotspot above 500 hPa (Figure 4a).

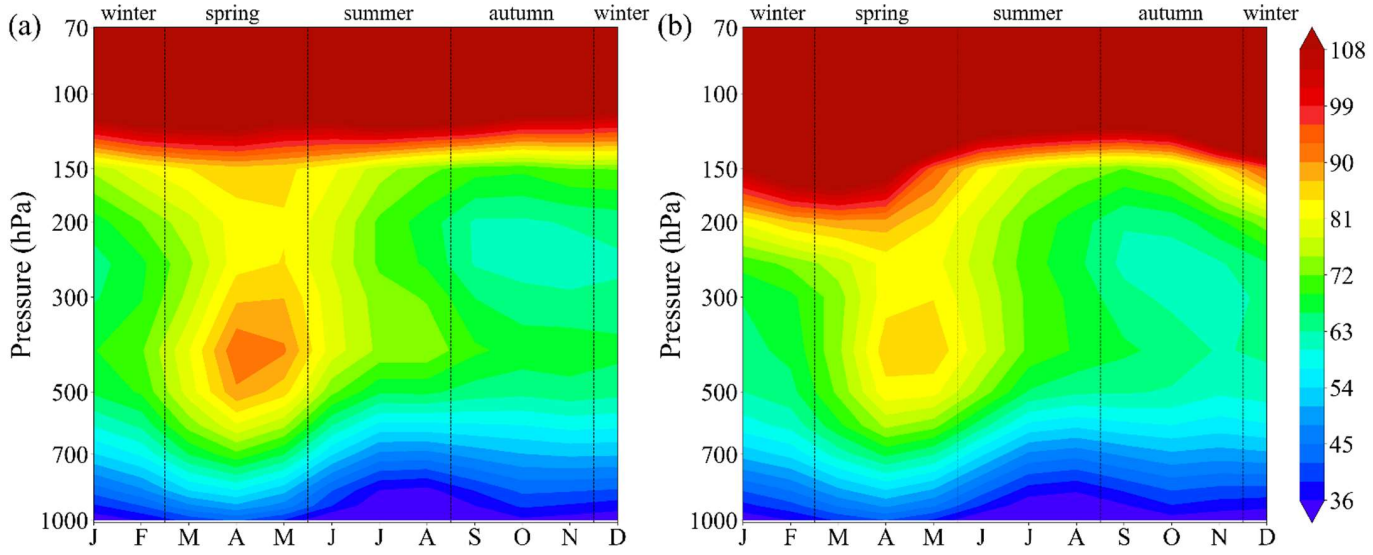

Figure 3. AIRS satellite retrieval of averaged O_3 (ppbv) vertical profiles for different months (spring: MAM, summer: JJA, autumn: SON, and winter: DJF) over (**a**) Yunnan province and (**b**) the 16°–36°N, 85°–125°E region from 2003 to 2023.

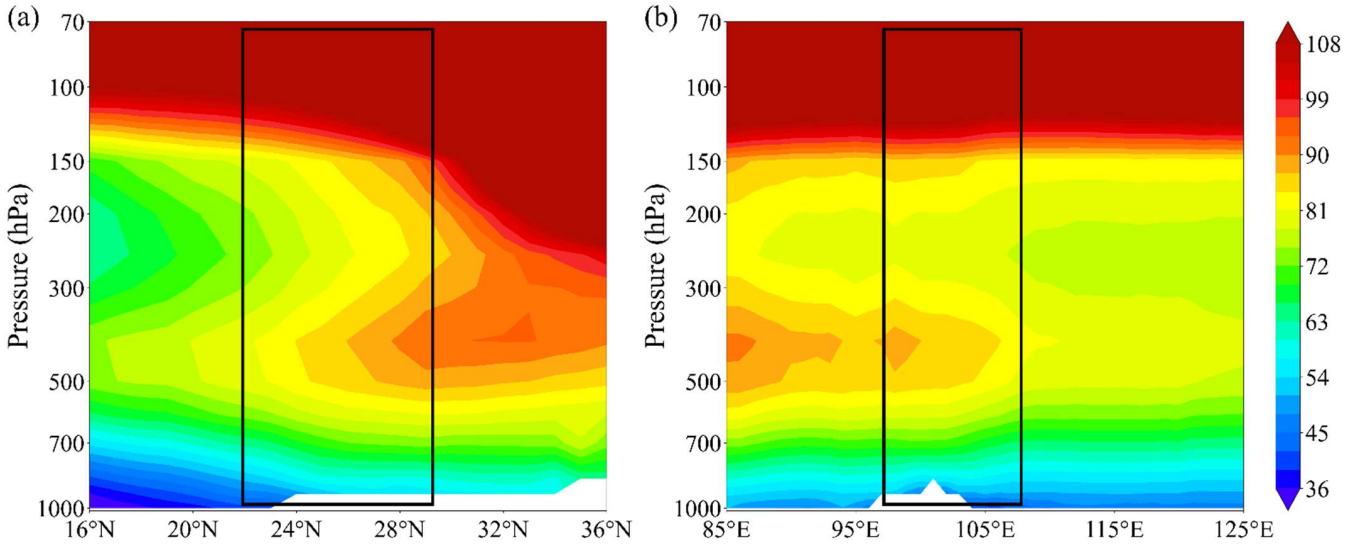

Figure 4. (**a**) Pressure–longitude cross-sections across the range of latitudes within Yunnan and (**b**) pressure-latitude cross-sections across the range of longitudes within Yunnan for averaged O_3 (ppbv) using data from the AIRS satellite dataset in spring from 2003 to 2023. The black boxes denote the location of Yunnan.

Figure 4b shows a band of O_3-enriched air extending from Northern India to Yunnan above 500 hPa, possibly indicating that cross-border BB transport exacerbates O_3 pollution in the lower troposphere. Figure 5d–f depicts the spatial distribution of O_3 and wind fields at altitudes of 303 hPa, 512 hPa, and 713 hPa, confirming the existence of the hotspot above 500 hPa. The strong westerly jet at 313 hPa and 512 hPa provides favorable meteorological conditions for the horizontal transport of pollutants from the source area in Myanmar to Yunnan, indirectly supporting the possibility that cross-border BB transport affects the formation of O_3 hotspots (Figure 5e,f). Figure S4 shows that Kunming and Xishuangbanna's five and four major pathways have been identified. The trajectories from central Myanmar have the highest proportion, accounting for 58.98% in Kunming and 38% in Xishuangbanna, further indicating the influence of cross-border BB on pollutants in Yunnan. Consequently, cross-border BB transport in the lower troposphere may further exacerbate tropospheric O_3 pollution.

The higher O_3 concentrations in the lower troposphere of Yunnan may also be attributable to the region's topographical conditions, as its elevated altitude facilitates the transport of stratospheric O_3 closer to the surface layer. A comprehensive analysis of satellite data has revealed that SIs and cross-border BB transport are two significant sources influencing air quality in the Yunnan region. However, there are still large uncertainties in studies of the quantitative regulation mechanism of springtime O_3 pollution over Yunnan.

3.2. Occurrence of SIs and the Cross-Border BB Transport in Yunnan

Satellite observations have confirmed the significant impact of SIs and cross-border BB transport on air quality during spring in Yunnan. However, the specific mechanisms and quantifications of each process have not been thoroughly investigated. This knowledge gap undermines the effectiveness of strategies aimed at reducing anthropogenic emissions. Many studies have demonstrated the accuracy of WACCM simulations and their applications in research related to O_3 and CO pollution [58–60]. WACCM simulations were performed to investigate the governing dynamic mechanisms of SIs and cross-border BB transport from 2020 to 2023.

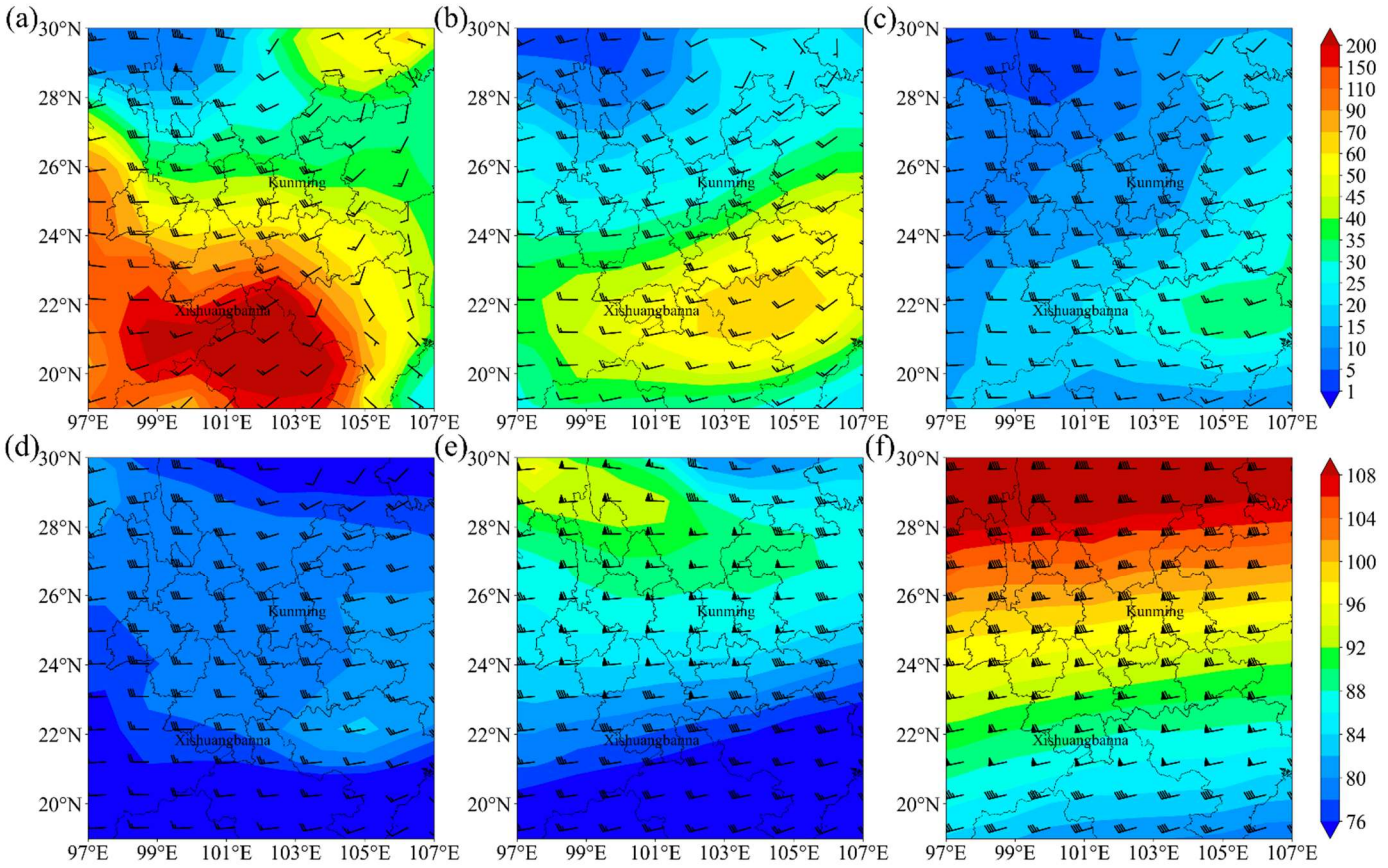

Figure 5. Spatial distribution of averaged $PM_{2.5}$ (μg/m^3) at (**a**) surface, (**b**) 810 hPa, and (**c**) 713 hPa, and O_3 (ppbv) at (**d**) 713 hPa, (**e**) 512 hPa, and (**f**) 303 hPa using data from WACCM over Yunnan in spring from 2020 to 2023.

In Figure 6, noticeable seasonal characteristics were observed for $PM_{2.5}$, CO, and CO01 concentrations in both Yunnan and Myanmar, where high values all occurred in later winter and early spring (February–April). In comparison, the high $PM_{2.5}$ and CO values in Yunnan are primarily concentrated between 800 hPa and the surface layer, while pollutants in Myanmar accumulate closer to the ground. Additionally, the maximum $PM_{2.5}$ and CO concentrations in Myanmar can reach 191 μg/m^3 and 1768 ppbv, whereas in Yunnan, these values reach 73 μg/m^3 and 679 ppbv (Figure 6). This indicates that Yunnan is situated downwind from Myanmar and is significantly influenced by cross-border BB transport. The vertical distribution characteristics of CO01 further confirm this inference. Many previous studies have demonstrated that the prevailing southwest winds in spring over ICP transport $PM_{2.5}$ to Yunnan, which is located downwind [16,18]. A hotspot of $PM_{2.5}$, CO, and CO01 concentrations was noticed between 700 and 800 hPa over Guangdong (Figure 6c,f,i), which indicated the important role of BB in air quality in that area [35].

Figure 7 further provides a time–height cross-section plot of monthly mean O_3 and O_3S profiles for Yunnan, Myanmar, India, and Guangdong from 2020 to 2023. A tongue-shaped plume of high O_3 exceeding 108 ppbv is transported downward to 500 hPa. A pool of O_3 with concentrations higher than 90 ppbv appears above the boundary layer. However, the vertical distribution characteristics of O_3S indicate that SIs have a relatively limited impact on the high concentrations of lower tropospheric O_3 in Yunnan and Myanmar. In comparison with the distribution of $PM_{2.5}$ and CO, both CO01 and O_3 in Yunnan exhibit high-value areas at 900 hPa, indicating that BB also plays a significant role in the accumulation of pollutants in this layer (Figure 6a,e). In Guangdong, the intensity of SIs is relatively weak, with less than 30 ppbv O_3S transported to the troposphere. In addition,

topography may be another factor influencing the contribution of SIs in Yunnan. The higher altitude facilitates the transport of stratospheric O_3 to the surface layer.

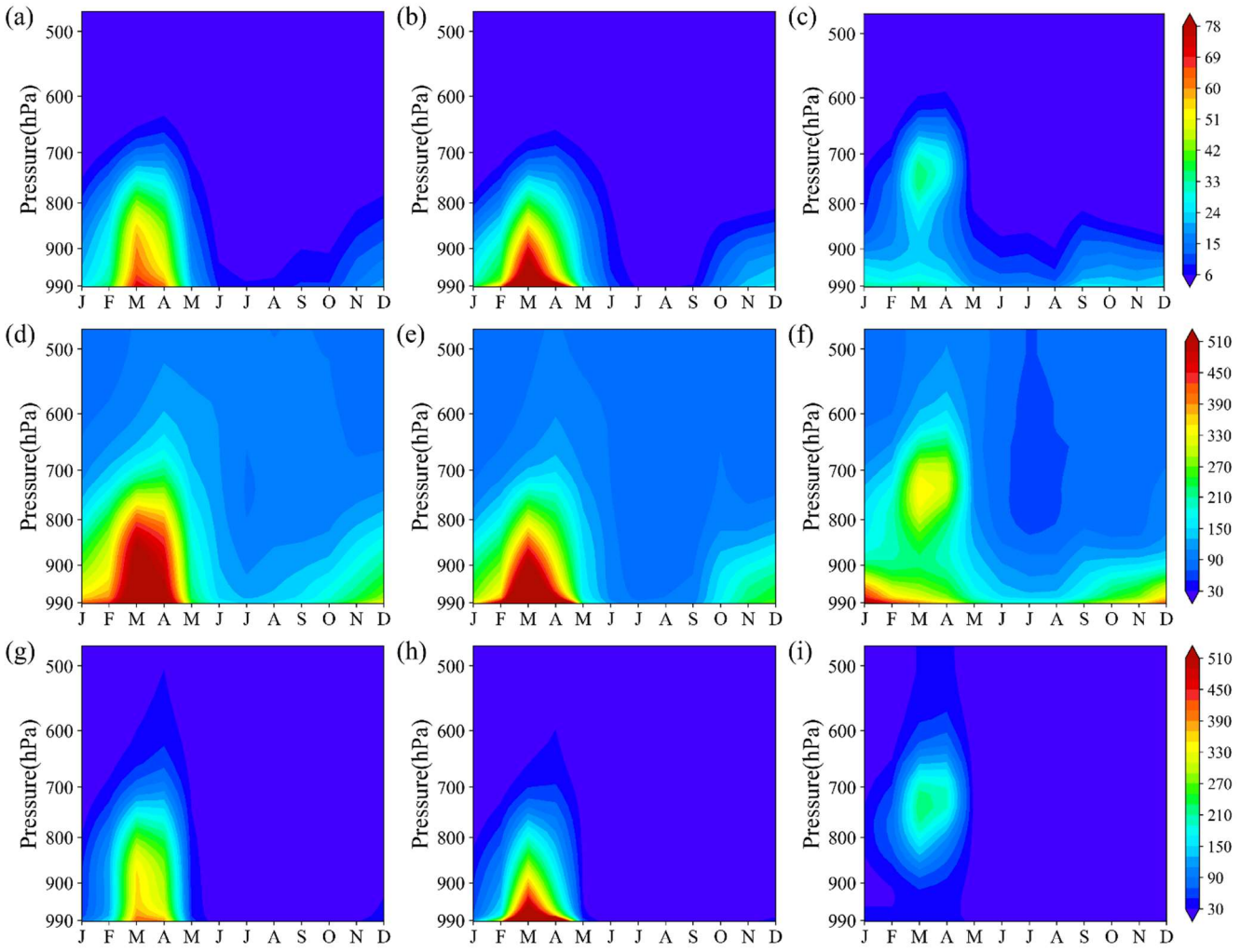

Figure 6. Temporal vertical profiles of averaged (**a**–**c**) $PM_{2.5}$ (μg/m^3), (**d**–**f**) CO, and (**g**–**i**) CO01 (ppbv) using data from WACCM over (**a**,**d**,**g**) Yunnan, (**b**,**e**,**h**) Myanmar, and (**c**,**f**,**i**) Guangdong from 2020 to 2023.

Notably, unlike the vertical distribution of pollutants in Yunnan and Myanmar, the pollutant hotspots in Guangdong were elevated in altitude but did not extend to the ground. Many studies have shown that there are two main reasons why these pollutant hotspots are elevated in altitude in Guangdong: the long-range horizontal transport of pollutants generated from BB in ICP and cross-latitudinal SI transport [26,35,61,62]. In our previous study, a strong inversion layer observed above the ABL blocked O_3 from penetrating the boundary layer in Hong Kong. Under favorable atmospheric circulation conditions (i.e., Saddle Point or Col), O_3 plumes can penetrate the boundary layer and affect the near-surface [21,26]. The differences between the WACCM-modeled O_3 concentration and the AIRS measurements are primarily due to inaccuracies in the WACCM simulations and AIRS measurements. Firstly, limitations in the vertical resolution of the WACCM simulations and parameterization schemes hinder accurate depictions of atmospheric layer variations, leading to inaccuracies [63]. Secondly, the vertical satellite data are derived from O_3 column concentrations, which may introduce errors during the inversion process. Therefore, more vertical observations need to be conducted to assess the WACCM simulation results and AIRS satellite data in the future [64].

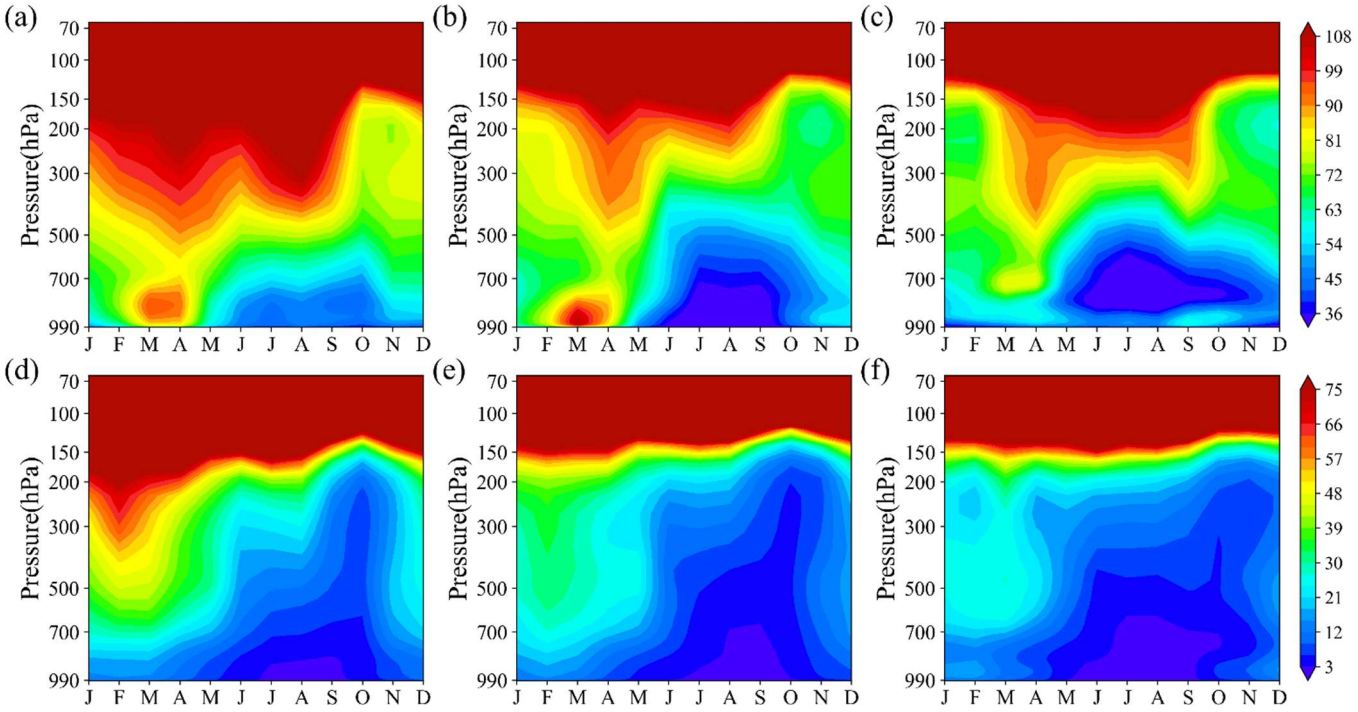

Figure 7. Temporal vertical profiles of averaged (**a**–**c**) O_3 (ppbv) and (**d**–**f**) O_3S (ppbv) using data from WACCM over (**a**,**d**) Yunnan, (**b**,**e**) Myanmar, and (**c**,**f**) Guangdong from 2020 to 2023.

Overall, our results indicate that SIs and cross-border BB transport are two major key mechanisms for determining spatiotemporal variations in $PM_{2.5}$ and O_3 in Yunnan during spring.

3.3. Mechanisms of SIs and Cross-Border BB Transport

Surface $PM_{2.5}$ reaches its maximum in Xishuangbanna, Eastern Myanmar, Northern Laos, and Northwestern Vietnam and gradually decreases along the northeastern direction, as shown in Figure 5. As altitude increases, $PM_{2.5}$ and O_3 concentrations exhibit opposite trends. Owing to topographical effects, the influence of cross-border BB transport is limited in higher-altitude areas. Conversely, the vertical downward transport of O_3 from the stratosphere is more likely to reach the surface layer in higher-altitude regions, resulting in an increase in O_3 concentrations with elevation. As mentioned in the previous section, cross-border BB transport may exacerbate $PM_{2.5}$ pollution in Yunnan during the spring.

Figure 8 shows pressure–longitude cross-sections along 23°N and 26°N for averaged $PM_{2.5}$ and vertical circulation in spring from 2020 to 2023. Owing to the impact of BB, high $PM_{2.5}$ concentrates on the surface of Myanmar, with a value of 150 $\mu g/m^3$. In Yunnan, the wind speed and elevation gradually increase from south to north. Vertically, surface $PM_{2.5}$ concentrations decrease with increasing elevation. A stronger westerly jet transports $PM_{2.5}$ to the downstream area, and the towering, mountainous terrain hinders further byproduct transport from BB. Therefore, Xishuangbanna, which has the lowest elevation in Yunnan and is closest to Myanmar, faces severe $PM_{2.5}$ pollution challenges.

To further track potential sources of $PM_{2.5}$ pollution in Yunnan, the PSCF and CWT approaches embedded in the HYSPLIT model were used to track air pollutant source areas for the target cities, Kunming and Xishuangbanna. A higher WPSCF value indicates a higher likelihood of the region being a potential $PM_{2.5}$ source area. Figure 9a shows that, for Xishuangbanna, regions with WPSCF values greater than 0.4 are primarily located in Myanmar, covering nearly half of the country's area. Additionally, in the central part of Myanmar, the WPSCF value exceeds 0.6. This suggests that Myanmar is a substantial potential source area for $PM_{2.5}$ in Xishuangbanna, confirming the significant impact of cross-border BB transport on $PM_{2.5}$. Compared with Xishuangbanna, the impact of cross-border

BB transport on Kunming is much smaller. The high-WPSCF-value areas for Kunming are mainly located in the southwestern region of Yunnan province (Figure 9b). Figure 9c,d show that the high-value WCWT areas are consistent with those for WPSCF. In spring, Myanmar serves as a potential source area for Xishuangbanna, with $PM_{2.5}$ contributions reaching 40–55 μg/m^3. Meanwhile, the $PM_{2.5}$ contribution to Kunming mainly falls within a range of 20–40 μg/m^3, with high-value areas primarily located in the southwestern region of Yunnan province and at the southwestern border of Yunnan with Myanmar. The spatial heterogeneity of WPSCF and WCWT between Xishuangbanna and Kunming is essentially driven by the difference in elevation (1.1 km for Xishuangbanna and 2.0 km for Kunming).

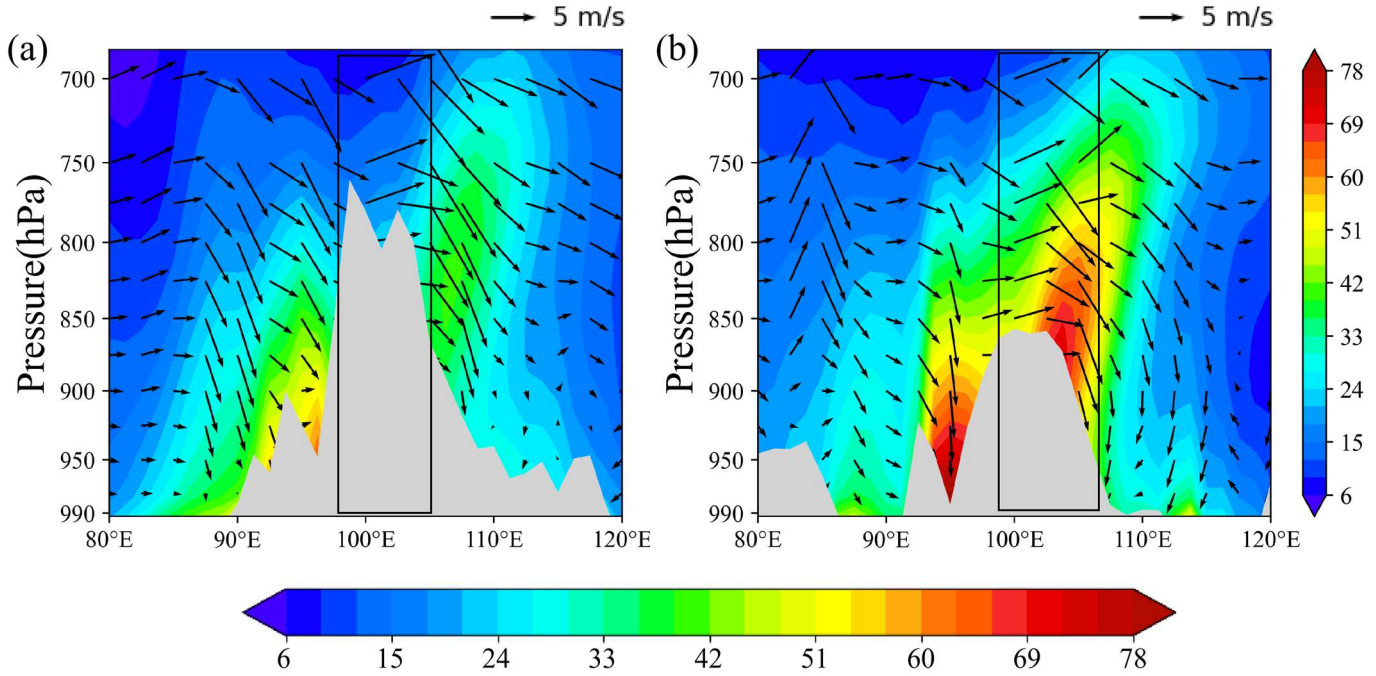

Figure 8. Pressure–longitude cross-sections along (**a**) 26°N and (**b**) 23°N for averaged $PM_{2.5}$ (μg/m^3) and vertical circulation using data from WACCM in spring from 2020 to 2023. The grey areas represent the altitude. The black boxes denote the location of Yunnan.

To further evaluate the relative SI contribution, we analyzed the horizontal distribution characteristics of the O_3S/O_3 ratio at different altitudes, which is used to describe the percentage of O_3 transported from the stratosphere to different levels. At a certain level, a higher ratio value of O_3S/O_3 signifies the greater impact of SI on O_3 concentrations at this level. Figure 10 shows that the O_3S/O_3 ratio increases with altitude, which is consistent with the SI characteristics. At 713 hPa and 512 hPa, an O_3S/O_3 hotspot can be seen over Northwest Yunnan, which agrees with the topographic feature, as shown in Figure 1b. In the higher troposphere (i.e., 303 hPa), the ratio exhibits a zonal distribution, increasing with higher latitudes. On the one hand, the tropopause height decreases with increasing latitude. On the other hand, the tropopause folding frequency demonstrates a similar zonal distribution, which provides favorable dynamic conditions for SIs (Figure S5). Owing to the significant influence of the Qinghai–Tibet Plateau's topography, hot spots are centered in the northwest part of Yunnan. Therefore, the complex terrain of the Yunnan region will have a significant impact on pollutant transport, exerting opposing effects on SIs and cross-border BB transport.

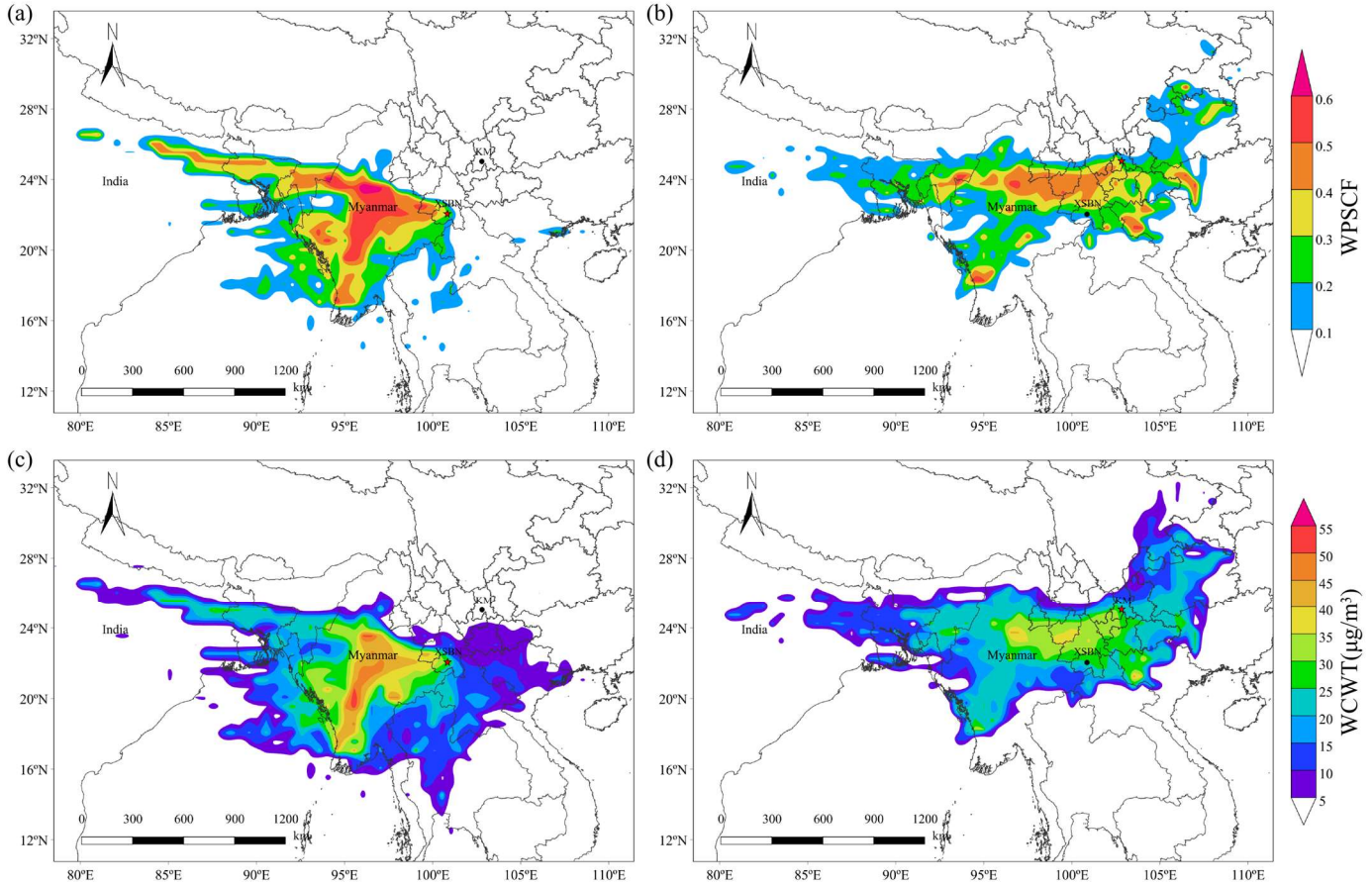

Figure 9. (**a**,**b**) Analysis of potential $PM_{2.5}$ source area from the surface in spring from 2020 to 2023 in different target cities: (**a**) Xishuangbanna; (**b**) Kunming. (**c**,**d**) Weight analysis of $PM_{2.5}$ concentrations ($\mu g/m^3$) in spring from 2020 to 2023 in different target cities: (**c**) Xishuangbanna; (**d**) Kunming.

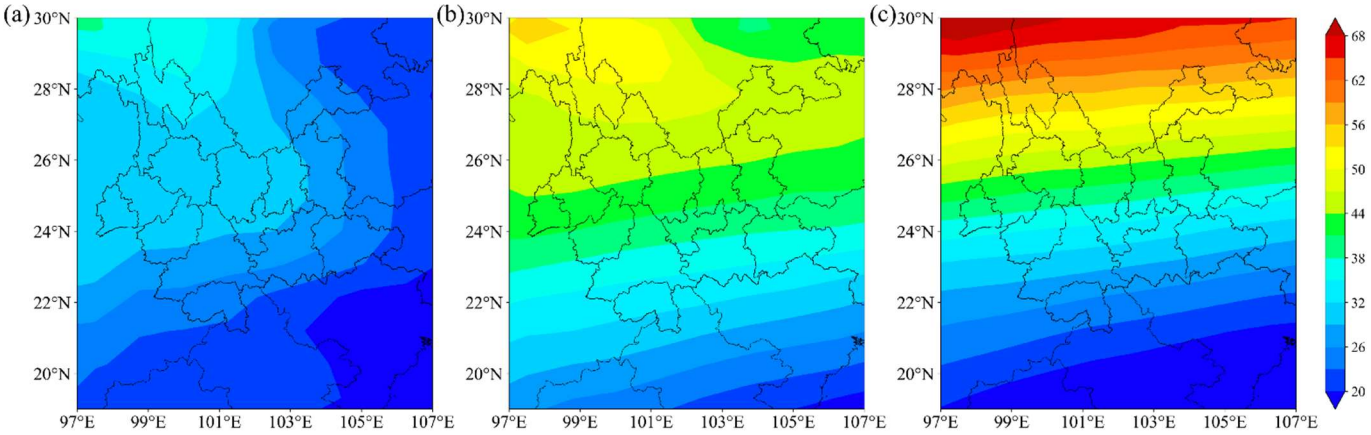

Figure 10. Spatial distribution of averaged O_3S/O_3 (%) using data from WACCM at (**a**) 713 hPa, (**b**) 512 hPa, and (**c**) 303 hPa over Yunnan in spring from 2020 to 2023.

3.4. Relationships between Topography and Air Pollutants

As discussed above, topography has a significant impact on pollutant transport in Yunnan. Thus, we expect that topography has a close relationship with O_3 and $PM_{2.5}$, which are examined in this section.

To explore the influence of topography, we analyzed the relationships between altitude and anomalous values of individual pollutant values during various months (February–

May) over Yunnan and Myanmar. The altitudes in Yunnan and Myanmar vary significantly. Yunnan has an average elevation of 2.3 km and a diverse internal topography, while Myanmar features predominantly gentle terrain, with most areas situated at elevations below 1 km. Figure 11 shows a strong negative relationship between altitude and anomalous $PM_{2.5}$ in Yunnan with an R higher than 0.67, which indicates that the effect of cross-border transport is gradually weakened by increasing altitude. In comparison, the connection between altitude and the cross-border transport impacts of BB in Myanmar is not prominently evident. This is primarily due to the lower altitudes in Myanmar and the predominantly local sources of BB. The significant negative correlation between CO (CO01) and altitude further substantiates the substantial impact of cross-border BB transport on air quality in Yunnan (Figure S6). The significant positive correlation between O_3S and altitude in Yunnan indicates that stratospheric O_3-enriched air is more readily transported downward to reach high-altitude cities. At the same time, the differences in R and slope between different months also prove the varying intensity of the influence of SIs and cross-border BB transport on $PM_{2.5}$ and O_3 at different altitudes. Areas at lower altitudes are more susceptible to $PM_{2.5}$ impacts from horizontal transport because of BB, while higher-altitude regions are more influenced by vertical O_3 transport from SIs.

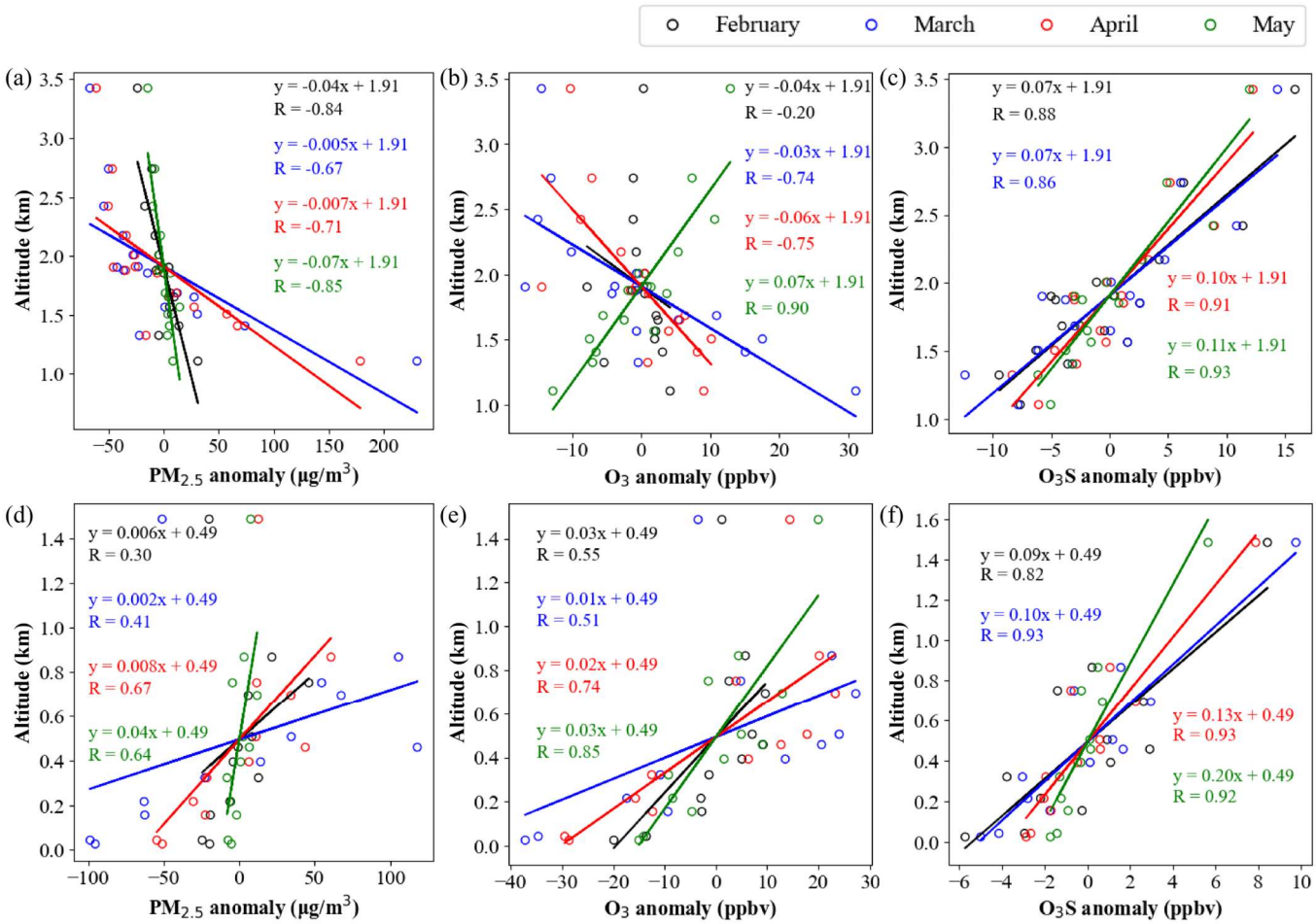

Figure 11. Scatter plots and linear fitting lines between altitude and (**a**,**d**) $PM_{2.5}$ ($\mu g/m^3$), (**b**,**e**) O_3 (ppbv), (**c**,**f**) O_3S (ppbv) from February to May in (**a**–**c**) Yunnan and (**d**–**f**) Myanmar.

Owing to the severe polluted status in March–April, we calculated the averaged March–April $PM_{2.5}$, O_3, and O_3S concentrations from 2020 to 2023 for 16 cities in Yunnan. We then sorted them by altitude, from highest to lowest (Figure 12). A close link between O_3, O_3S, $PM_{2.5}$, and topography was found. As the altitude decreases, there is a signifi-

cant increase in $PM_{2.5}$ concentration and a decrease in the proportion of O_3S. Under the influence of topography, SIs can contribute 8–31 ppbv to surface O_3 in these cities. Notably, Xishuangbanna, the closest city in Yunnan to BB sites, has a further higher $PM_{2.5}$ (close to 300 $\mu g/m^3$) than other cities (100–200 $\mu g/m^3$), resulting from cross-border BB transport.

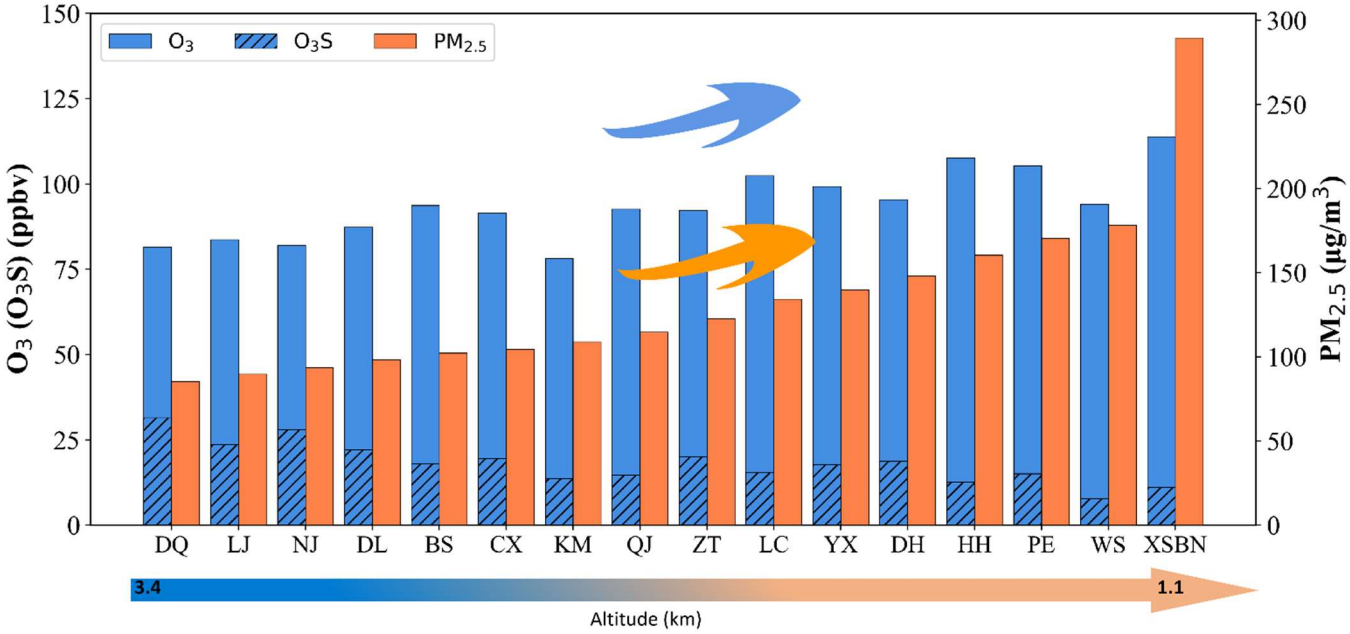

Figure 12. Averaged $PM_{2.5}$ ($\mu g/m^3$), O_3 (ppbv), and O_3S (ppbv) concentrations of 16 cities in Yunnan from March to April.

It should be noted that the WACCM products cannot directly track the impact of cross-border BB transport on O_3. Therefore, it is not possible to calculate the quantitative contribution of cross-border BB transport using WACCM data. Furthermore, the less significant trends observed in O_3 and O_3S can be attributed to the absence of constraints on surface O_3 and O_3S in the simulation results. As a workaround, O_3 and O_3S from levels close to surface pressure were used as substitutes for surface concentrations.

4. Discussion

Currently, Yunnan province faces severe $PM_{2.5}$ and O_3 pollution in the spring. A comprehensive analysis of MODIS and AIRS satellite data over the past 21 years has revealed the presence of two atmospheric pollutant transport processes associated with springtime in Yunnan, specifically SIs and BB. The implementation of APCAAP in 2013 led to a reduction in local emissions, amplifying the relative contribution of two unique transport processes during springtime.

In this study, we focused on assessing the impact of SIs and BB on O_3 and $PM_{2.5}$ during the spring season in Yunnan. Two factors affecting SIs and cross-border BB transport were identified: the prevalent southwest winds and complex topographical conditions. Yunnan is situated in the downwind region of Myanmar and features complex terrain. This unique geographical position provides an ideal environment for SIs and the cross-border transport of BB emissions, allowing $PM_{2.5}$ and O_3 from Myanmar to be transported to Yunnan. The complex topography within Yunnan, with higher elevations in the north and lower elevations in the south, facilitates the easier transport of $PM_{2.5}$ to border cities with lower elevations, such as Xishuangbanna. Cities farther from Myanmar, owing to higher elevations, obstruct some $PM_{2.5}$ transport, weakening cross-border BB transport and resulting in the spatial distribution of $PM_{2.5}$ concentrations decreasing with elevation.

High-frequency tropopause folding in Yunnan provides favorable dynamic conditions for SIs. The distribution of O_3 and O_3S exhibits a northwest-southeast trend similar to the

terrain. This can be partly attributed to the higher tropopause folding frequency in the northwest, influenced by the Qinghai–Tibet Plateau, as well as the high-altitude terrain in the northwest, which facilitates the transport of stratospheric O_3 to the surface. The contribution of SIs to surface O_3 in Yunnan's cities ranges from 6 to 31 ppbv, accounting for 10% to 38% of surface O_3.

Notably, these two unique natural processes in Yunnan contribute differently to surface O_3 and $PM_{2.5}$ concentrations during springtime. SIs are solely responsible for the downward transport of stratospheric O_3, thereby contributing to surface O_3 pollution. High-altitude sites are more susceptible to the effects of SIs, as evidenced by the positive correlation between O_3S and altitude. Conversely, the cross-border BB transport affects both O_3 and $PM_{2.5}$ concentrations through the transport of $PM_{2.5}$, O_3, and O_3 precursors. The impact of cross-border BB transport on O_3 and $PM_{2.5}$ decreases with increasing altitude owing to topographic obstruction, as indicated by the negative correlation between altitude and O_3 as well as $PM_{2.5}$. Moreover, it should be noted that in addition to the processes mentioned above (see also [65]), the temporal evolution of the tropopause height (e.g., foldings) exhibits persistent behavior (memory effect). This means that a small fluctuation in the past is followed by a drastically enhanced fluctuation in the future. The response time varies from 4 months to 6 years [66]. This behavior has also been found in surface O_3, $PM_{2.5,}$ and AOD [67].

This study underscores the significant regulatory role of SIs and cross-border BB transport as non-local emissions on local $PM_{2.5}$ and O_3 pollution in Yunnan, which will pose a substantial challenge for policymakers in the future. Hence, we recommend that the impact of these two distinct natural transport processes be taken into consideration when formulating local emission reduction strategies. It is essential to comprehensively consider the influence of terrain conditions on pollutant transport in cities at different altitudes.

Supplementary Materials: The following supporting information can be downloaded at: https://www.mdpi.com/article/10.3390/rs16132409/s1, Figure S1: Time series of modeled and observed O_3 (ppbv), $PM_{2.5}$ ($\mu g/m^3$) and AOD in various cities across Yunnan province; Figure S2: Box plots of observed (a) $PM_{2.5}$ ($\mu g/m^3$), (b) PM_{10} ($\mu g/m^3$), (c) O_3 ($\mu g/m^3$) and (d) 550 nm AOD in different seasons from 2015 to 2023. The red lines depict the change in the annual mean of $PM_{2.5}$, PM_{10} and AOD from 2015 to 2023; Figure S3: Scatter plots and linear fitting lines between AOD and (a) $PM_{2.5}$ ($\mu g/m^3$), (b) PM10 ($\mu g/m^3$) in various seasons from 2015 to 2023 in Yunnan; Figure S4: Backward trajectory clusters identified by HYSPLIT simulations in different target cities: (a) Xishuangbanna and (b) Kunming in spring from 2020 to 2023; Figure S5: Spatial distribution of tropopause folding frequency in spring from 2001 to 2019; Figure S6: Scatter plots and liner fitting lines between (a,c) CO (ppbv) and (b,d) CO01 (ppbv) from February to May in (a,b) Yunnan and (c,d) Myanmar; Table S1: Statistical evaluation of monthly averaged O_3, $PM_{2.5}$ and AOD concentration.

Author Contributions: Conceptualization, P.L. and K.Z.; methodology, P.L.; software, P.L.; validation, K.Z.; formal analysis, P.L. and K.Z.; investigation, P.L. and K.Z.; resources, P.L.; data curation, P.L.; writing—original draft preparation, P.L.; writing—review and editing, K.Z. and Z.Y.; visualization, Z.Y.; supervision, Z.Y.; project administration, K.Z.; funding acquisition, Z.Y. and K.Z. All authors have read and agreed to the published version of the manuscript.

Funding: This research was funded by National Natural Science Foundation of China, grant number 42105164; The Key-Area Research and Development Program of Guangdong Province, grant number 2020B1111360003; The Open Research Fund Program of Plateau Atmosphere and Environment Key Laboratory of Sichuan Province, grant number PAEKL-2024-K01; Yunnan Science and Technology Department Youth Project 202401AU070202; Guangdong Basic and Applied Basic Research Foundation, grant number 2022A1515011078; Xianyang key research and development program, grant number L2022ZDYFSF040.

Data Availability Statement: The original contributions presented in the study are included in the article and supplementary material, further inquiries can be directed to the corresponding author.

Acknowledgments: We thank NASA for providing datasets of MODIS and AIRS. We also thank NCAR for providing datasets of WACCM.

Conflicts of Interest: The authors declare no conflicts of interest. The funders had no role in the design of the study; in the collection, analyses, or interpretation of data; in the writing of the manuscript; or in the decision to publish the results.

References

1. Shao, T.; Wang, P.; Yu, W.; Gao, Y.; Zhu, S.; Zhang, Y.; Hu, D.; Zhang, B.; Zhang, H. Drivers of alleviated PM2.5 and O3 concentrations in China from 2013 to 2020. *Resour. Conserv. Recycl.* **2023**, *197*, 107110. [CrossRef]
2. Wang, N.; Lyu, X.; Deng, X.; Huang, X.; Jiang, F.; Ding, A. Aggravating O(3) pollution due to NO(x) emission control in eastern China. *Sci. Total Environ.* **2019**, *677*, 732–744. [CrossRef] [PubMed]
3. van Zelm, R.; Preiss, P.; van Goethem, T.; Van Dingenen, R.; Huijbregts, M. Regionalized life cycle impact assessment of air pollution on the global scale: Damage to human health and vegetation. *Atmos. Environ.* **2016**, *134*, 129–137. [CrossRef]
4. Belis, C.A.; Van Dingenen, R.; Klimont, Z.; Dentener, F. Scenario analysis of PM(2.5) and ozone impacts on health, crops and climate with TM5-FASST: A case study in the Western Balkans. *J. Environ. Manag.* **2022**, *319*, 115738. [CrossRef] [PubMed]
5. Zhang, Y.; Yang, Y.; Zhang, L.; Xu, H.; Sun, J.; Wang, T.; Li, F.; Chang, X.; Ho, S.S.H.; Li, B.; et al. Insight into the contributions of primary emissions of sulfate, nitrate, and ammonium from residential solid fuels to ambient PM2.5. *Atmos. Res.* **2023**, *290*, 106790. [CrossRef]
6. Yu, X.; Zhang, Y.; Liu, N.; Yang, S. Characteristics of Secondary PM2.5 Under Different Photochemical Reactivity Backgrounds in the Pearl River Delta Region. *Front. Environ. Sci.* **2022**, *10*, 837158. [CrossRef]
7. Hughes, D.D.; Christiansen, M.B.; Milani, A.; Vermeuel, M.P.; Novak, G.A.; Alwe, H.D.; Dickens, A.F.; Pierce, R.B.; Millet, D.B.; Bertram, T.H.; et al. PM2.5 chemistry, organosulfates, and secondary organic aerosol during the 2017 Lake Michigan Ozone Study. *Atmos. Environ.* **2021**, *244*, 117939. [CrossRef]
8. Xie, Y.; Liu, Z.; Wen, T.; Huang, X.; Liu, J.; Tang, G.; Yang, Y.; Li, X.; Shen, R.; Hu, B.; et al. Characteristics of chemical composition and seasonal variations of PM(2.5) in Shijiazhuang, China: Impact of primary emissions and secondary formation. *Sci. Total Environ.* **2019**, *677*, 215–229. [CrossRef] [PubMed]
9. Yang, W.; Chen, H.; Wu, J.; Wang, W.; Zheng, J.; Chen, D.; Li, J.; Tang, X.; Wang, Z.; Zhu, L.; et al. Characteristics of the source apportionment of primary and secondary inorganic PM(2.5) in the Pearl River Delta region during 2015 by numerical modeling. *Environ. Pollut.* **2020**, *267*, 115418. [CrossRef] [PubMed]
10. Song, X.; Jia, J.; Wu, F.; Niu, H.; Ma, Q.; Guo, B.; Shao, L.; Zhang, D. Local emissions and secondary pollutants cause severe PM(2.5) elevation in urban air at the south edge of the North China Plain: Results from winter haze of 2017-2018 at a mega city. *Sci. Total Environ.* **2022**, *802*, 149630. [CrossRef] [PubMed]
11. Chen, C.; Qiu, Y.; Xu, W.; He, Y.; Li, Z.; Sun, J.; Ma, N.; Xu, W.; Pan, X.; Fu, P.; et al. Primary Emissions and Secondary Aerosol Processing During Wintertime in Rural Area of North China Plain. *J. Geophys. Res. Atmos.* **2022**, *127*, e2021JD035430. [CrossRef]
12. Jin, X.; Cai, X.; Yu, M.; Song, Y.; Wang, X.; Kang, L.; Zhang, H. Diagnostic analysis of wintertime PM2.5 pollution in the North China Plain: The impacts of regional transport and atmospheric boundary layer variation. *Atmos. Environ.* **2020**, *224*, 117346. [CrossRef]
13. Xiao, Z.; Miao, Y.; Du, X.; Tang, W.; Yu, Y.; Zhang, X.; Che, H. Impacts of regional transport and boundary layer structure on the PM2.5 pollution in Wuhan, Central China. *Atmos. Environ.* **2020**, *230*, 117508. [CrossRef]
14. Shan, M.; Wang, Y.; Lu, Y.; Liang, C.; Wang, T.; Li, L.; Li, R.Y.-M. Uncovering PM2.5 transport trajectories and sources at district within city scale. *J. Cleaner Prod.* **2023**, *423*, 138608. [CrossRef]
15. Zhao, S.; Yu, Y.; Qin, D.; Yin, D.; Dong, L.; He, J. Analyses of regional pollution and transportation of PM2.5 and ozone in the city clusters of Sichuan Basin, China. *Atmos. Pollut. Res.* **2019**, *10*, 374–385. [CrossRef]
16. Yang, Q.; Zhao, T.; Tian, Z.; Kumar, K.R.; Chang, J.; Hu, W.; Shu, Z.; Hu, J. The Cross-Border Transport of PM2.5 from the Southeast Asian Biomass Burning Emissions and Its Impact on Air Pollution in Yunnan Plateau, Southwest China. *Remote Sens.* **2022**, *14*, 1886. [CrossRef]
17. Zhang, Z.; Wang, X.; Cheng, S.; Guan, P.; Zhang, H.; Shan, C.; Fu, Y. Investigation on the difference of PM2.5 transport flux between the North China Plain and the Sichuan Basin. *Atmos. Environ.* **2022**, *271*, 118922. [CrossRef]
18. Luo, Y.; Wei, H.; Yang, K. The impact of biomass burning occurred in the Indo-China Peninsula on PM2.5 and its spatiotemporal characteristics over Yunnan Province. *Sci. Total Environ.* **2024**, *908*, 168185. [CrossRef] [PubMed]
19. Lupaşcu, A.; Otero, N.; Minkos, A.; Butler, T. Attribution of surface ozone to NOx and volatile organic compound sources during two different high ozone events. *Atmos. Chem. Phys.* **2022**, *22*, 11675–11699. [CrossRef]
20. Kang, M.; Zhang, H.; Ying, Q. Enhanced summertime background ozone by anthropogenic emissions—Implications on ozone control policy and health risk assessment. *Atmos. Environ.* **2023**, *314*, 120116. [CrossRef]
21. Zhao, K.; Huang, J.; Wu, Y.; Yuan, Z.; Wang, Y.; Li, Y.; Ma, X.; Liu, X.; Ma, W.; Wang, Y.; et al. Impact of Stratospheric Intrusions on Ozone Enhancement in the Lower Troposphere and Implication to Air Quality in Hong Kong and Other South China Regions. *J. Geophys. Res. Atmos.* **2021**, *126*, e2020JD033955. [CrossRef]
22. Hu, F.; Xie, P.; Tian, X.; Xu, J.; Li, A.; Lupascu, A.; Butler, T.; Hu, Z.; Lv, Y.; Zhang, Z.; et al. Integrated analysis of the transport process and source attribution of an extreme ozone pollution event in Hefei at different vertical heights: A case of study. *Sci. Total Environ.* **2024**, *906*, 167237. [CrossRef] [PubMed]

23. Wang, X.; Zhang, H.; Hong, X.; Xiang, Y.; Wang, S.; Zhang, T.; Qin, Z.; Ou, J. Vertical profiles and regional transport of ozone in typical area of Yangtze-Huaihe River Basin during the autumn base on multiple lidars. *Atmos. Pollut. Res.* **2024**, *15*, 101983. [CrossRef]
24. Li, D.; Bian, J.; Fan, Q. A deep stratospheric intrusion associated with an intense cut-off low event over East Asia. *Sci. China Earth Sci.* **2014**, *58*, 116–128. [CrossRef]
25. Bartusek, S.; Wu, Y.; Ting, M.; Zheng, C.; Fiore, A.; Sprenger, M.; Flemming, J. Higher-Resolution Tropopause Folding Accounts for More Stratospheric Ozone Intrusions. *Geophys. Res. Lett.* **2023**, *50*, e2022GL101690. [CrossRef]
26. Zhao, K.; Hu, C.; Yuan, Z.; Xu, D.; Zhang, S.; Luo, H.; Wang, J.; Jiang, R. A modeling study of the impact of stratospheric intrusion on ozone enhancement in the lower troposphere over the Hong Kong regions, China. *Atmos. Res.* **2021**, *247*, 105158. [CrossRef]
27. Phanikumar, D.V.; Niranjan Kumar, K.; Bhattacharjee, S.; Naja, M.; Girach, I.A.; Nair, P.R.; Kumari, S. Unusual enhancement in tropospheric and surface ozone due to orography induced gravity waves. *Remote Sens. Environ.* **2017**, *199*, 256–264. [CrossRef]
28. Liu, C.; He, C.; Wang, Y.; He, G.; Liu, N.; Miao, S.; Wang, H.; Lu, X.; Fan, S. Characteristics and mechanism of a persistent ozone pollution event in Pearl River Delta induced by typhoon and subtropical high. *Atmos. Environ.* **2023**, *310*, 119964. [CrossRef]
29. Ding, H.; Kong, L.; You, Y.; Mao, J.; Chen, W.; Chen, D.; Chang, M.; Wang, X. Effects of tropical cyclones with different tracks on ozone pollution over the Pearl River Delta region. *Atmos. Res.* **2023**, *286*, 106680. [CrossRef]
30. Shu, Z.; Zhao, T.; Chen, Y.; Liu, Y.; Yang, F.; Jiang, Y.; He, G.; Yang, Q.; Zhang, Y. Terrain effect on atmospheric process in seasonal ozone variation over the Sichuan Basin, Southwest China. *Environ. Pollut.* **2023**, *338*, 122622. [CrossRef]
31. Ali, M.A.; Huang, Z.; Bilal, M.; Assiri, M.E.; Mhawish, A.; Nichol, J.E.; de Leeuw, G.; Almazroui, M.; Wang, Y.; Alsubhi, Y. Long-term PM(2.5) pollution over China: Identification of PM(2.5) pollution hotspots and source contributions. *Sci. Total Environ.* **2023**, *893*, 164871. [CrossRef] [PubMed]
32. Van Haver, P.; De Muer, D.; Beekmann, M.; Mancier, C. Climatology of tropopause folds at midlatitudes. *Geophys. Res. Lett.* **1996**, *23*, 1033–1036. [CrossRef]
33. Zhu, J.; Xia, X.; Che, H.; Wang, J.; Zhang, J.; Duan, Y. Study of aerosol optical properties at Kunming in southwest China and long-range transport of biomass burning aerosols from North Burma. *Atmos. Res.* **2016**, *169*, 237–247. [CrossRef]
34. Lin, C.-Y.; Hsu, H.-m.; Lee, Y.H.; Kuo, C.H.; Sheng, Y.-F.; Chu, D.A. A new transport mechanism of biomass burning from Indochina as identified by modeling studies. *Atmos. Chem. Phys.* **2009**, *9*, 7901–7911. [CrossRef]
35. Zeng, X.; Li, S.; Xing, J.; Yang, J.; Wang, Q.; Song, G.; Teng, M.; Zhou, D.; Lu, J. CALIPSO-observed Southeast Asia biomass-burning influences on aerosol vertical structure in Guangdong-Hong Kong-Macao Greater Bay Area. *Atmos. Res.* **2023**, *289*, 106755. [CrossRef]
36. Engel-Cox, J.A.; Holloman, C.H.; Coutant, B.W.; Hoff, R.M. Qualitative and quantitative evaluation of MODIS satellite sensor data for regional and urban scale air quality. *Atmos. Environ.* **2004**, *38*, 2495–2509. [CrossRef]
37. Jin, X.; Holloway, T. Spatial and temporal variability of ozone sensitivity over China observed from the Ozone Monitoring Instrument. *J. Geophys. Res. Atmos.* **2015**, *120*, 7229–7246. [CrossRef]
38. Midhuna, T.M.; Gharai, B.; Jose, S.; Rao, P.V.N. Study on Regional Variations of Aerosol Loading Using Long Term Satellite Data Over Indian Region. *J. Indian Soc. Remote Sens.* **2016**, *45*, 685–697. [CrossRef]
39. Lee, E.; Županski, M.; Županski, D.; Park, S.K. Impact of the OMI aerosol optical depth on analysis increments through coupled meteorology–aerosol data assimilation for an Asian dust storm. *Remote Sens. Environ.* **2017**, *193*, 38–53. [CrossRef]
40. Zhang, M.; Su, B.; Bilal, M.; Atique, L.; Usman, M.; Qiu, Z.; Ali, M.A.; Han, G. An Investigation of Vertically Distributed Aerosol Optical Properties over Pakistan Using CALIPSO Satellite Data. *Remote Sens.* **2020**, *12*, 2183. [CrossRef]
41. Shaik, D.S.; Kant, Y.; Mitra, D.; Singh, A.; Chandola, H.C.; Sateesh, M.; Babu, S.S.; Chauhan, P. Impact of biomass burning on regional aerosol optical properties: A case study over northern India. *J. Environ. Manag.* **2019**, *244*, 328–343. [CrossRef] [PubMed]
42. Stachlewska, I.; Samson, M.; Zawadzka, O.; Harenda, K.; Janicka, L.; Poczta, P.; Szczepanik, D.; Heese, B.; Wang, D.; Borek, K.; et al. Modification of Local Urban Aerosol Properties by Long-Range Transport of Biomass Burning Aerosol. *Remote Sens.* **2018**, *10*, 412. [CrossRef]
43. Xiong, X.; Liu, X.; Wu, W.; Knowland, K.E.; Yang, Q.; Welsh, J.; Zhou, D.K. Satellite observation of stratospheric intrusions and ozone transport using CrIS on SNPP. *Atmos. Environ.* **2022**, *273*, 118956. [CrossRef]
44. Liu, J.; Wang, S.; Yuan, Q.; Zhang, F.; Zhu, L. Vertical Profile of Ozone Derived from Combined MLS and TES Satellite Observations. *Remote Sens.* **2022**, *14*, 1588. [CrossRef]
45. Ma, P.; Mao, H.; Zhang, J.; Yang, X.; Zhao, S.; Wang, Z.; Li, Q.; Wang, Y.; Chen, C. Satellite monitoring of stratospheric ozone intrusion exceptional events—A typical case of China in 2019. *Atmos. Pollut. Res.* **2022**, *13*, 101297. [CrossRef]
46. Levy, R.C.; Mattoo, S.; Munchak, L.A.; Remer, L.A.; Sayer, A.M.; Patadia, F.; Hsu, N.C. The Collection 6 MODIS aerosol products over land and ocean. *Atmos. Meas. Tech.* **2013**, *6*, 2989–3034. [CrossRef]
47. Sayer, A.M.; Hsu, N.C.; Bettenhausen, C.; Jeong, M.J.; Meister, G. Effect of MODIS Terra radiometric calibration improvements on Collection 6 Deep Blue aerosol products: Validation and Terra/Aqua consistency. *J. Geophys. Res. Atmos.* **2015**, *120*, 12157–12174. [CrossRef]
48. Aumann, H.H.; Chahine, M.T.; Gautier, C.; Goldberg, M.D.; Kalnay, E.; McMillin, L.M.; Revercomb, H.; Rosenkranz, P.W.; Smith, W.L.; Staelin, D.H.; et al. AIRS/AMSU/HSB on the Aqua Mission: Design, Science Objectives, Data Products, and Processing Systems. *IEEE Trans. Geosci. Remote Sens.* **2003**, *41*, 253–264. [CrossRef]

49. Wei, J.; Li, Z.; Peng, Y.; Sun, L. MODIS Collection 6.1 aerosol optical depth products over land and ocean: Validation and comparison. *Atmos. Environ.* **2019**, *201*, 428–440. [CrossRef]
50. Polissar, A.V.; Hopke, P.K.; Harris, J.M. Source Regions for Atmospheric Aerosol Measured at Barrow, Alaska. *Environ. Sci. Technol.* **2001**, *35*, 4214–4226. [CrossRef] [PubMed]
51. *Ambient Air Quality Standards: GB 3095-2012*; General Administration of Quality Supervision, Inspection and Quarantine of the People's Republic of China, Standardization Administration of China. China Standards Press: Beijing, China, 2012.
52. Chen, Y.; Li, D.; Karimian, H.; Wang, S.; Fang, S. The relationship between air quality and MODIS aerosol optical depth in major cities of the Yangtze River Delta. *Chemosphere* **2022**, *308*, 136301. [CrossRef] [PubMed]
53. Jia, C.; Sun, L.; Zhang, X.; Wang, Y. Verification of Mcd19a2 Data and Study of Aerosol Characteristics in Beijing-Tianjin-Hebei Region. *ISPRS Ann. Photogramm. Remote Sens. Spat. Inf. Sci.* **2020**, *3*, 675–679. [CrossRef]
54. Wang, J.; Zhao, B.; Wang, S.; Yang, F.; Xing, J.; Morawska, L.; Ding, A.; Kulmala, M.; Kerminen, V.M.; Kujansuu, J.; et al. Particulate matter pollution over China and the effects of control policies. *Sci. Total Environ.* **2017**, *584–585*, 426–447. [CrossRef] [PubMed]
55. Kong, L.; Xin, J.; Zhang, W.; Wang, Y. The empirical correlations between PM2.5, PM10 and AOD in the Beijing metropolitan region and the PM2.5, PM10 distributions retrieved by MODIS. *Environ. Pollut.* **2016**, *216*, 350–360. [CrossRef]
56. Xu, J.; Han, F.; Li, M.; Zhang, Z.; Du, X.; Wei, P. On the opposite seasonality of MODIS AOD and surface PM2.5 over the Northern China plain. *Atmos. Environ.* **2019**, *215*, 116909. [CrossRef]
57. Chen, J.; Xin, J.; An, J.; Wang, Y.; Liu, Z.; Chao, N.; Meng, Z. Observation of aerosol optical properties and particulate pollution at background station in the Pearl River Delta region. *Atmos. Res.* **2014**, *143*, 216–227. [CrossRef]
58. Weimer, M.; Kinnison, D.E.; Wilka, C.; Solomon, S. Effects of denitrification on the distributions of trace gas abundances in the polar regions: A comparison of WACCM with observations. *Atmos. Chem. Phys.* **2023**, *23*, 6849–6861. [CrossRef]
59. Dong, J.; Zhang, X.; Zhan, N. Satellite-based estimates of high-resolution CO concentrations at ground level in the Yangtze River Economic Belt of China. *Atmos. Environ.* **2023**, *312*, 120018. [CrossRef]
60. Liang, T.; Luo, J.; Zhang, C.; Tian, H.; Bai, Z.; Bian, J.; Wang, Z.; Luo, F.; Zhu, F.; Mao, L.; et al. The impact of tropopause fold event on surface ozone concentration over Tibetan Plateau in July. *Atmos. Res.* **2024**, *298*, 107156. [CrossRef]
61. Jian, Y.; Fu, T.M. Injection heights of springtime biomass-burning plumes over peninsular Southeast Asia and their impacts on long-range pollutant transport. *Atmos. Chem. Phys.* **2014**, *14*, 3977–3989. [CrossRef]
62. Zhao, K.; Chen, Y.; Lian, P.; Li, W.; Yang, F.; Zhang, X.; Yang, R. Impact of stratospheric intrusions on surface ozone enhancement in Hong Kong in the lower troposphere: Implications for ozone control strategy. *Atmos. Environ.* **2024**, *329*, 120539. [CrossRef]
63. Lamarque, J.-F.; Kinnison, D.E.; Mills, M.J.; Marsh, D.R.; Calvo, N.; Polvani, L.M. Climate Change from 1850 to 2005 Simulated in CESM1(WACCM). *J. Clim.* **2013**, *26*, 7372–7391. [CrossRef]
64. Rawat, P.; Naja, M.; Fishbein, E.; Thapliyal, P.K.; Kumar, R.; Bhardwaj, P.; Jaiswal, A.; Tiwari, S.N.; Venkataramani, S.; Lal, S. Performance of AIRS ozone retrieval over the central Himalayas: Use of ozonesonde and other satellite datasets. *Atmos. Meas. Tech.* **2023**, *16*, 889–909. [CrossRef]
65. Varotsos, C.; Ondov, J.; Tzanis, C.; Öztürk, F.; Nelson, M.; Ke, H.; Christodoulakis, J. An observational study of the atmospheric ultra-fine particle dynamics. *Atmos. Environ.* **2012**, *59*, 312–319. [CrossRef]
66. Varotsos, C.; Efstathiou, M.; Tzanis, C. Scaling behaviour of the global tropopause. *Atmos. Chem. Phys.* **2009**, *9*, 677–683. [CrossRef]
67. Varotsos, C.; Efstathiou, M.; Tzanis, C.; Deligiorgi, D. On the limits of the air pollution predictability: The case of the surface ozone at Athens, Greece. *Environ. Sci. Pollut. Res. Int.* **2012**, *19*, 295–300. [CrossRef] [PubMed]